Received: 6 August 2024 | Revised: 19 September 2024 | Accepted: 16 October 2024

DOI: 10.1111/jace.20241

Journal of the American Ceramic Society

RESEARCH ARTICLE

Laboratory and synchrotron x-ray micro–computed tomography to shed light on degradation features of corroded Roman glass

Roberta Zanini[1] | **Giulia Franceschin**[1] | **Luisa Vigorelli**[2,3] | **Gianluca Iori**[4] | **Lara Chiaberge**[3] | **Elena Longo**[5] | **Laura Guidorzi**[3] | **Alessandro Re**[3] | **Alessandro Lo Giudice**[3] | **Arianna Traviglia**[1]

[1]Istituto Italiano di Tecnologia, Center for Cultural Heritage Technology (CCHT), Venezia-Mestre, Italy

[2]Dipartimento di Fisica "G. Occhialini", Università di Milano Bicocca, Milan, Italy

[3]Dipartimento di Fisica, Università di Torino e INFN, sezione di Torino, Turin, Italy

[4]SESAME - Synchrotron-light for Experimental Science and Applications in the Middle East, Allan, Jordan

[5]Elettra Sincrotrone Trieste S.C.p.A, Basovizza, Trieste, Italy

Correspondence
Roberta Zanini and Arianna Traviglia, Istituto Italiano di Tecnologia, Center for Cultural Heritage Technology (CCHT), Venezia-Mestre, Italy.
Email: roberta.zanini@iit.it and arianna.traviglia@iit.it

Abstract

This study explores the three-dimensional structure of Roman glass through the combined use of laboratory and phase-contrast synchrotron x-ray micro–computed tomography. This original approach validates a noninvasive analytical procedure designed to enhance the understanding of glass degradation mechanisms, crucial for the preservation of historical artefacts. The high-resolution images obtained reveal the intricate internal structure and morphology of various forms of glass deterioration, including cracking, pitting, and the formation of multilayered iridescent patinas. The research provides compelling evidence of corrosion processes and interaction mechanisms with burial soil, shedding light on the chemical and physical interactions that occur over centuries. By characterizing and examining the long-term alteration of ancient glass, this work contributes to the field of archaeometry, offering insights into how different types of glass withstand the test of time in diverse environmental conditions. The findings have important implications for conservation strategies, enabling better preservation techniques for glass artefacts.

KEYWORDS

burial alteration, cultural heritage, glass corrosion, micro–computed tomography, synchrotron

1 | INTRODUCTION

Glass corrosion, influenced by intrinsic factors such as material composition and extrinsic agents such as environmental conditions, remains a complex and debated topic despite widespread recognition. Understanding of the degradation processes in natural environments is still progressing, and the interplay of environmental factors in glass corrosion is not entirely clear, even after extensive research.[1–6] Recent research has shown that analyzing real-life instances of prolonged glass degradation could greatly improve our comprehension of underlying mechanisms and assist in formulating effective strategies to address glass corrosion.

The ultimate aim of this study is to investigate the formation mechanisms of various degradation features observed on ancient glass, exploring how environmental interactions influence these features within

archaeological strata. The objective is to validate a non-invasive experimental method utilizing laboratory x-ray micro–computed tomography (μCT) and phase contrast synchrotron x-ray micro–computed tomography (SR-μCT) to reveal the three-dimensional (3D) material structure of altered glass. This involves examining multiple archaeological glass samples displaying different alteration marks.

Distinct macroscopic alteration marks observed on archaeological glass indicate specific alteration mechanisms.[6,7] "Weathering" is associated with surface deterioration caused by water interaction, resulting in the leaching of alkaline and alkaline earth ions (Na^+ and Ca^{2+}) from the glass network. These ions react with compounds in the environment, precipitating alteration products on the glass surface,[4] progressively weakening and dissolving the glass network. This process gives rise to various visible features of alteration that develop on the glass surface, influenced by different parameters such as glass compositions, temperature, water availability, pH, and so forth.[8–12]

Until now, research on glass corrosion has predominantly centered on contemporary glass types, primarily those used in industrial and commercial contexts. However, exploring ancient glass offers a unique opportunity to expand our understanding of corrosion mechanisms. Ancient glasses, altered by centuries of environmental phenomena exposure and varied burial conditions, offer a wealth of information. By studying these historical artefacts, researchers can gain insights into long-term alteration processes and the complex interaction among glass composition, environmental factors, and degradation over time.[13] This investigation not only aids in preserving cultural heritage, but also provides valuable knowledge for modern materials science.

To date, investigating ancient glass corrosion has posed challenges due to limitations in diagnostic techniques.[14] Often, achieving a comprehensive analysis entails invasive sampling, which may not always be feasible; thus, observations are often confined to surface-level assessments. Moreover, the highly heterogeneous nature of constituent materials and corrosion products, coupled with the diverse shapes and size of cultural heritage objects, necessitates specialized experimental setups and meticulous selection of investigative methods.[15,16] Nondestructive techniques, like x-ray radiography and computed tomography (CT), offer valuable insights into an object's inner structure and composition.[17–19] Comparative analysis using laboratory and synchrotron μCT highlights the benefits of utilizing synchrotron radiation and conventional sources in a complementary manner, while lab-μCT enables comprehensive scanning of larger objects, SR-μCT (phase contrast) captures essential microstructural details.

In this study, the integration of laboratory-based and synchrotron-based μCT analyses enabled to gain multi-scale insights into the structural alterations of two distinct types of archaeological glass. This approach, applied to an iridescent sample, aided in the characterization of the thickness, shape, and separation of each layer composing the 3D superficial iridescent patina. μCT images of samples affected by cracking provided detailed 3D information on the size, morphology, and distribution of cracks within the sample bulk. This facilitated understanding the mechanisms of crack formation and appreciating the effects of the interaction between glass and burial environment during the alteration processes.

Thus, the findings of this study shed light on centuries-long interactions between glass, its components, and burial environments. Such insights are important for advancing research aimed at comprehending both the processes of glass corrosion and the development of effective preservation techniques.

2 | METHODS

The glass fragments examined in this study were discovered on the plough soil surface in the countryside of the ancient Roman city of Aquileia (North-Eastern Italy) during archaeological field-walking survey activities undertaken in 2012 and in 2017.[20]

All the glass samples exhibit the typical composition of Roman silica-soda-lime glass, which was produced using *natron* (sodium carbonate, Na_2CO_3) as a flux. Specifically, this type of glass typically contains 60–75 wt% silica, 15–20 wt% soda, and 5–10 wt% lime. More details about the glass samples and the conditions of finding are reported in Supporting Information.

Samples were accurately selected to display the main forms of deterioration that commonly affect archaeological glass, including crack formation (samples 591612, 581755, and 2.2234), pitting (sample 591554), and presence of an iridescent patina on the surface (sample 581681) (Figure 1).

Sample 591612 is a cobalt-blue rounded rim, samples 581755 and 2.2234 are green-blue and emerald-green glass beads, sample 591554 is a decolored wall, and sample 581681 is a black (very dark green) fragmentary flat base with wall, probably of a Roman inkwell.

2.1 | CT setups

The samples were morphologically characterized by combining laboratory CT instrumentation and high-resolution SR-μCT. Overview scans (one for each sample) were performed using the laboratory setup. Subsequently, selected areas of interest were identified for each sample and

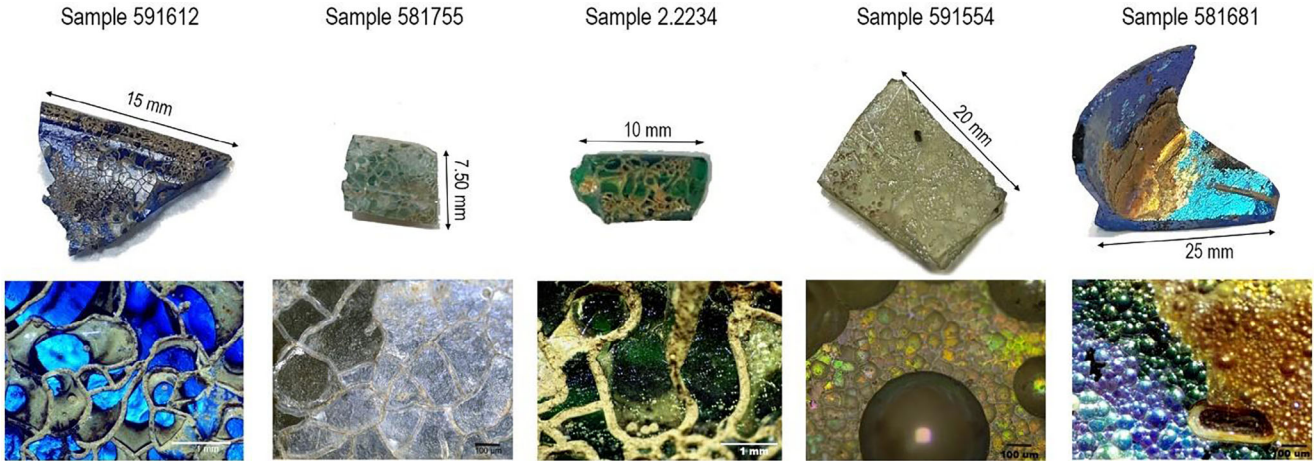

FIGURE 1 Digital photographs of the samples analyzed using x-ray micro–computed tomography (top); optical microscope images of the alteration features that affect the archaeological glass samples (bottom).

scanned at higher spatial resolution using synchrotron radiation. These μCT scans were performed by rotating the sample over multiple angles.

2.1.1 | Laboratory μCT setup

A custom-designed μCT setup, housed at the Physics Department of the University of Torino and developed in collaboration with the Italian National Institute for Nuclear Physics (INFN), was employed to meet the high-resolution imaging requirements of the project's objectives, thanks to the OpenAIAr laboratory access call by the Italian Archaeometric Society (AIAr).[21] This equipment, thanks to its versatility and the different components available in terms of source, detector, and mechanics, has already confirmed its suitability for investigating samples of very different sizes and materials.[22–28]

The x-ray source used to irradiate archaeological glass is the Microfocus L8121-03 manufactured by Hamamatsu. The beryllium emission window is 200-μm thick and it is oriented toward the sample. The irradiation cone has an angle of 43° approximately, and the minimum source–object distance is 17 mm, this being the intended distance between focal spot and beryllium window. The detector is a Teledyne Dalsa Shad-o-Box 6K HS, a flat panel consisting of a 2304 × 2940 pixel matrix corresponding to an active area of 11.4 × 14.6 cm^2. Each detector pixel has an area of 49.5 × 49.5 μm^2, and consists of a CsI direct contact scintillator, a photodiode, and a CMOS transistor.

The specimen was mounted on a rotary stage (Newport URS50BPP) placed on a triangular support facilitating both mobility and adjustment of its inclination for the alignment procedure. The synchronization of the stage and the detector was managed through a custom GUI developed using the Labview software by National Instruments.

The following parameters were used for the acquisition:

- focal spot size of 7 μm, to achieve the best spatial resolution;
- x-ray tube voltage of 90 kV, to enable a reasonable transmission of x-rays considering the material and size of the analyzed samples;
- x-ray tube current of 111 μA (maximum value in these conditions), to minimize the acquisition time;
- integration time of 3 s/projection, to optimize the exploitation of the 16 384 grey levels of the detector;
- angular step of rotation of 0.15°, resulting in a total number of projections equal to 2400.

The source–object-detector distances chosen for sample analysis are reported in Table 1.

During the acquisition phase, the sample was placed inside a polystyrene support, a material chosen for its moderate attenuation of the x-ray energies employed in the scan. The holder was rotated 360° around its vertical axis with small angular increments (0.15°), and a radiograph was acquired for each of these positions. To perform flat field correction, 20 white beam images and 20 dark current images were collected.

2.1.2 | Synchrotron μCT setup

Synchrotron images were collected at the x-ray imaging beamline SYRMEP (Synchrotron Radiation Medical Physics) of Elettra Sincrotrone Trieste S.C.p.A., Italy.[29] The experiment was carried out in parallel beam geometry using a polychromatic x-ray beam (white/pink beam) filtered with 1.5 mm of Si and 3.5 mm of Al, achieving a peaked mean energy of 26.9 keV. Phase-contrast was obtained with free space propagation setting the

TABLE 1 Geometry used for the laboratory μCT analysis.

Sample	591612	581755	2.2234	581681[a]	591554
Source–detector (mm)			650		
Source–object (mm)			100		150
Object–detector (mm)			550		500
Magnification			6.5		4.3
Resulting penumbra (μm)			~39		~23
Voxel (μm)			~8		~11

[a]On this sample, a local tomography focused on the patina area was performed.

sample-to-detector distance 150 mm. The CT scans were accomplished collecting 1800 projections (i.e., sample radiographs) over 180°. In addition, 20 flat fields (i.e., background images) and 20 dark fields (i.e., dark images) were collected at the beginning and at the end of each μCT scan. The images were acquired with 2-s exposure time using an ORCA Flash 4.0 Hamamatsu sCMOS detector (2048 × 2048 pixels, physical pixel size 6.5 μm) with a 17-μm thick GGG scintillator screen. The detector, equipped with a zoom system, was able to collect images with an effective pixel size of 2 × 2 μm^2 or 1 × 1 μm^2 for some higher resolution details. The acquisition involved stitching together multiple vertical μCT scans, thereby extending the detector field-of-view to encompass either the size of the sample or a region of interest within it.

2.2 | Image processing

2.2.1 | Laboratory μCT images

The averaged images of the 20 white beam and the 20 dark current images have been calculated using MATLAB. The acquired projections were processed and flat field corrected using the software ParRec developed by the University of Bologna.[17] The reconstructions of the CT sections (32-bit TIFF files) were made using an FDK algorithm[30,31] available in the same software. The subsequent 3D rendering and images analysis were performed with the ORS Dragonfly software.[32] For the latter, volume segmentation was realized both with histogram-based (Otsu algorithm[33]) and morphological operation (i.e., region growing) methods.

2.2.2 | Synchrotron μCT images

Tomographic reconstructions were computed using the open-source software SYRMEP Tomo-Project.[29] Sinograms were pre-processed with an algorithm for ring artefacts compensation[34] (width parameter: 12 ÷ 35, depending on scan), and by retrieval of phase contrast information[35] (δ/β parameter: 50). 3D volumes were reconstructed as stacks of 16-bit TIFF files (slices). Image exploration and cropping were performed in Image-J.[36] The stitching of adjacent scans was performed with a custom Python script. Volume renderings and binary masks of glass, voids, and deposit material were obtained in ORS Dragonfly. Segmentation for the latter was achieved by analyzing the histogram of the image grey levels, followed by a sequence of morphological operations (i.e., image closing, opening, and voids filling).

3 | RESULTS

3.1 | Cracked samples

The CT setup enabled comprehensive scans of the two archaeological samples (591612 and 581755) with cracked surfaces. Within both samples, the cracks resulting from the corrosion process feature rounded ends, suggesting the possible influence of soil mechanics in fracturing the glass through erosion.

Several images obtained from the reconstruction of the sample 581755 are reported in Figure 2. The images highlight the dense network of fractures that covers the surface of the sample and affect its entire volume, occupying more than 10% of the glass object (Figure 2B). The slices reported in Figure 2C,D provide a view of the cracks in cross-section, allowing for the observation of their internal structure and size.

The cracks are approximately 0.1–0.5 mm wide. They are interconnected and propagate very deeply into the sample until they reach the central hole, which appears to be filled with material coming from the soil in which the glass fragments have been buried for centuries. The soil particles can be segmented based on their radiopacity and dimension. Certain fractures seem to initiate from the central hole and propagate toward the surface until they intersect with others originating from it.

Additionally, it is discernible that an area at the interface between the voids within the cracks and the glass volume exhibits a distinct grey level, indicating the

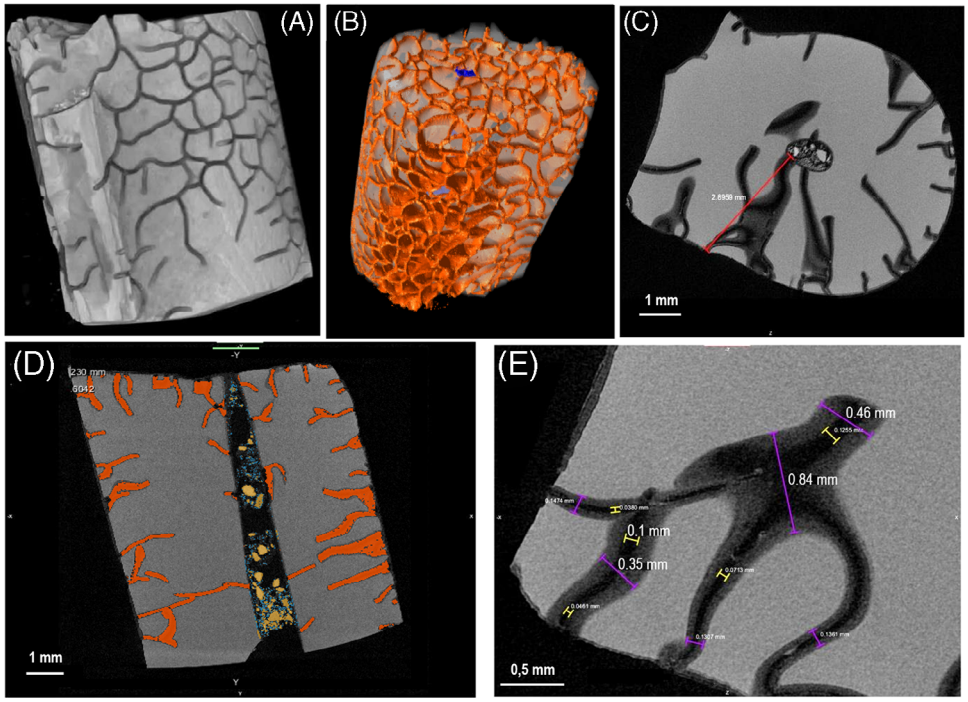

FIGURE 2 Laboratory µCT scan of the sample 581755. (A) 3D rendering; (B) volume overlap with mask of the cracks; (C) tomographic slice; (D) cross-section with overlap of different masks: orange mask for cracks, yellow mask for bigger and brighter grains of soil, and blue mask for smaller and darker grains of soil; (E) detail of the crack size measurement result.

potential presence of a material with a density different from the glass matrix. A material with a consistent texture seems to coat the entire glass fragment, as evidenced by the similar grey outline visible in Figure 2C–E. One plausible explanation for the nature of this material could be its association with the formation of a layer of hydrated silica due to the glass alteration process. The formation of this silica-rich layer can result from different process of glass alteration. In particular, two models of alteration-layer formation have been proposed and supported by various experimental evidence: (i) uniform dissolution of the glass into the aqueous phase, resulting in the precipitation of a low-solubility, silicon-rich phase; and (ii) selective dissolution of soluble components such as sodium, which is followed by the restructuring of the partially hydrated remaining network.[37–40] Such formation of a hydrated silica layer likely occurred on the sample 591612, both on the glass surface and within the extensive and deep cracks, where the crack walls provide additional surfaces where the alteration processes can occur.

The geometry of the cracking propagation observed through optical microscopy on the surface of the sample 591612 (Figure 1) appeared atypical, with cracks entirely filled with mineralized material, likely originating from the soil in which the object was buried for centuries. µCT images corroborated the existence of a dense adventitious material that partially or completely filled the cracks, while also facilitating the reconstruction of the 3D geometry of the cracks network (Figure 3). The cracks appear narrower compared to those found on sample 581755, occupying a smaller volume of the glass object (about 7.3%). Due to the low contrast between the glass and filling material, the crack shows irregular edges, which impact the quality of the segmentation.

Several filled cracks extend into the bulk, beneath the glass surface, as evident in the slices presented in Figure 3. Particularly, these slices reveal larger areas where mineralized material is present, displaying a leopard-like texture (indicated by the orange mask in Figure 3). Upon closer examination of the surface of the sample 591612 (Figure 1), it becomes apparent that these regions correspond to whitish areas visible on the glass fragment's surface. The images obtained from the tomographic analysis suggest that the material within the cracks, located beneath the initial superficial layer of the glass, imparts a whitish hue to the glass instead of its original blue color. The color observed on the sample surface with the naked eye, aligning with the leopard-spot areas, corresponds to the "soil" present within the cracks.

Sample 591612 was also analyzed using phase contrast SR-µCT to obtain higher resolution images of a portion of the glass fragment. A 3D volume reconstruction obtained from the SR-µCT data is reported in Figure 4A. The virtual sections derived from the SR-µCT reconstruction (Figure 4B,C) showcase the enhanced contrast of synchrotron phase-contrast images, providing a more detailed

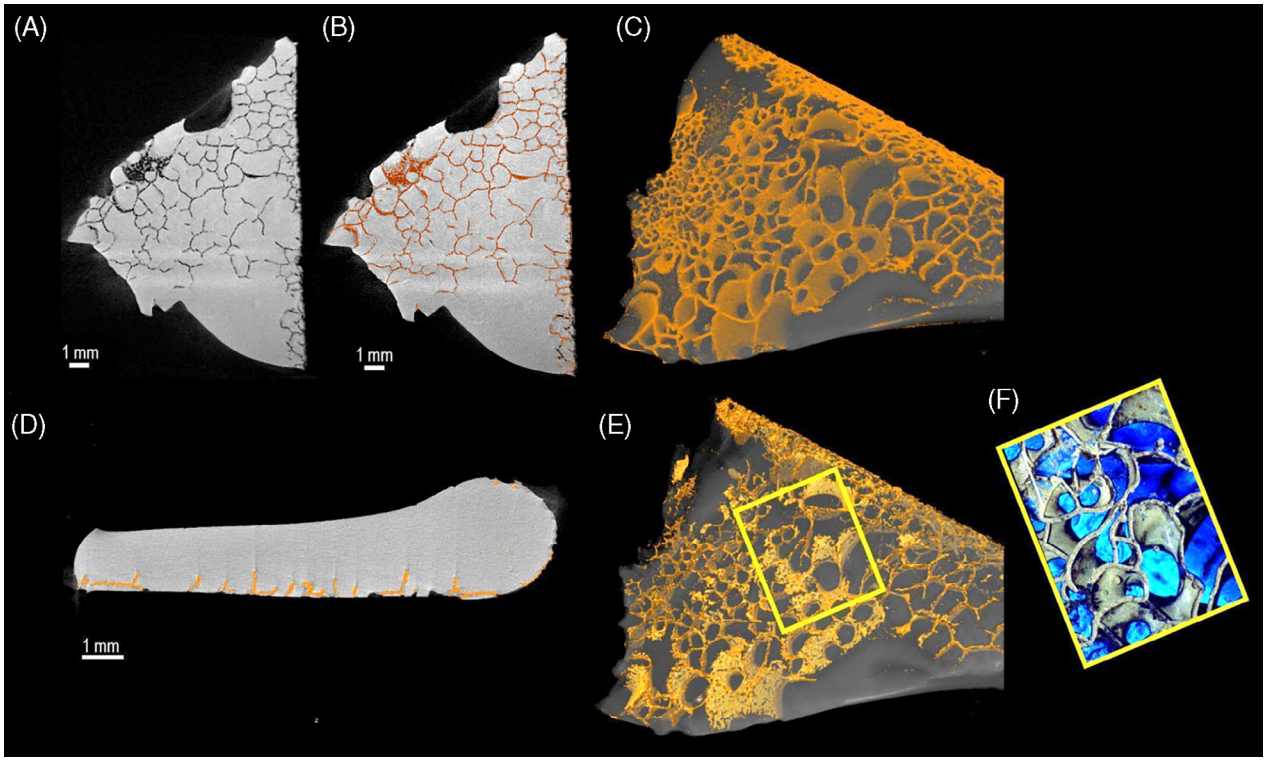

FIGURE 3 Laboratory μCT scan of the sample 591612. (A) Cracks network connected to the glass surface. (B) Segmented cracks (orange label). (C) 3D render of the sample with cracks network segmented in orange. (D) Horizontal slice where cracks penetration depth in the glass matrix is highlighted. (E and F) Corresponding detail of the glass alteration on the CT model and on visible light.

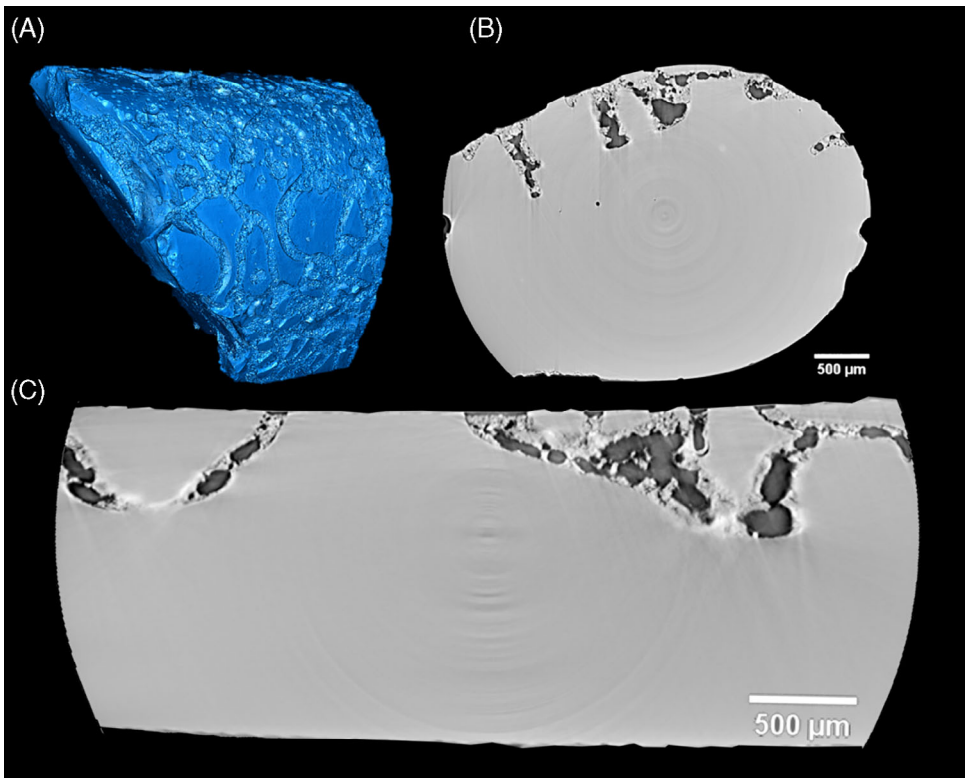

FIGURE 4 (A) 3D volume rendering of a corner of the cracked sample 591612 obtained from SR-μCT analyses; (B and C) virtual slices obtained from the volume of panel (a).

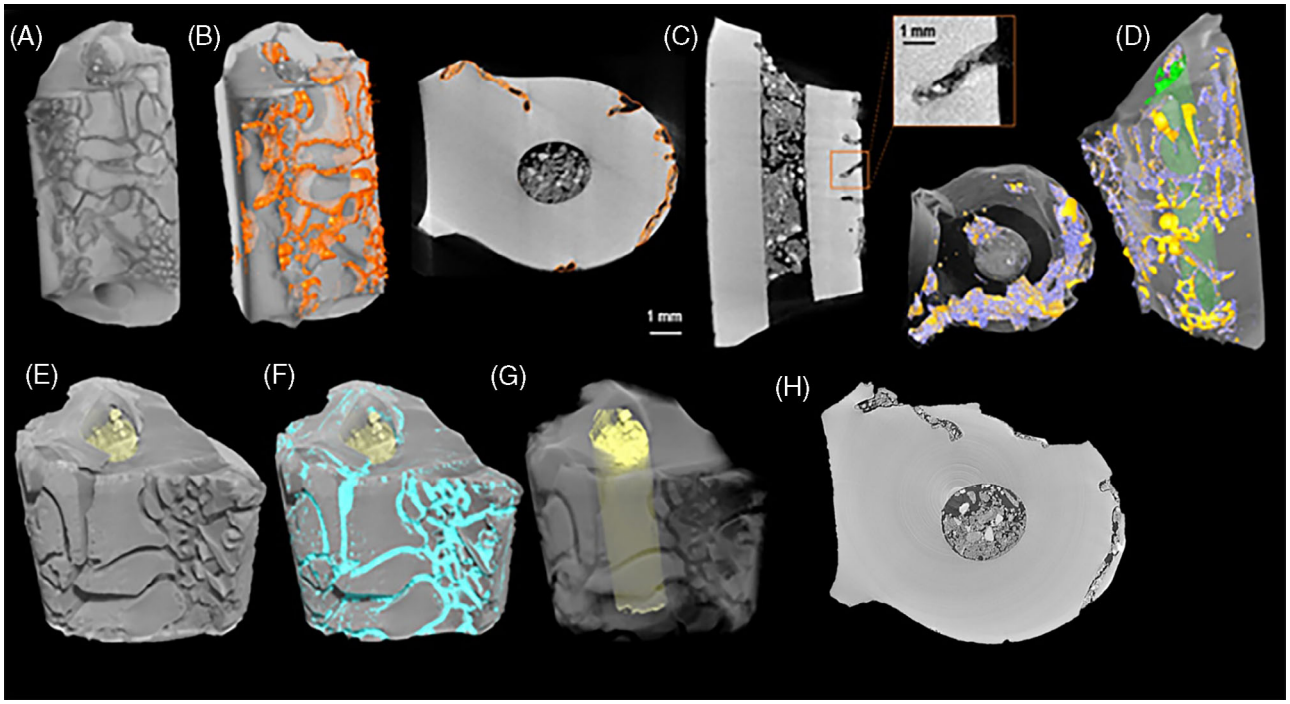

FIGURE 5 Images obtained from μCT analysis (top); images obtained from SR-μCT analysis (bottom). (A) 3D volume rendering of the entire sample 2.2234. (B) Orange mask to highlight the material filling the cracks. (C) Horizontal and vertical slices where the hole filling material is visible, with a detail of a crack where both air and filling material are present. (D) In green the material inside the central hole, in yellow the voids, and in purple the filling material in the cracks. (E) 3D volume rendering of a portion of the sample 2.2234 from SR-μCT. The material filling the internal hole of the sample is highlighted in yellow. Sediments filling the outer network of cracks have been digitally removed, uncovering the smooth, round bottom of U-shaped corrosion voids. (F) Light blue overlay of the soil and material filling the cracks on the sample surface. (G) Bulk glass in partial transparency, revealing the material inside the central hole (yellow). (H) Horizontal slice from SR-μCT where the individual particles constituting the sediment within the central hole of the sample are visible.

visualization of the material filling the fractures. The soil grains are distinctly visible, as are the regions within the cracks where air is present. Moreover, it is more apparent how the fractures interconnect beneath the surface of the glass, forming small fragments seemingly bound together by the soil, acting as a sort of cement. This information holds particular significance in the context of restoring a glass object under similar altered conditions, because it suggests that excessively cleaning the sample could lead to the removal of soil from the cracks, potentially resulting in the loss of material cohesion. This, in turn, might cause the breakage of small "islands" of glass that have formed on the surface.[41]

Similar results were obtained from μCT and SR-μCT analysis of the third cracked sample investigated (2.2234). The distinct phases composing this specimen (bulk glass material, void and cracked surfaces, soil deposit partially filling cavities and cracks) can be visualized in 3D on both μCT (Figure 5A–D) and SR-μCT datasets (Figure 5E–G). The volume occupied by cracks on the sample surface was analyzed using laboratory μCT images. This accounts for approximately 2% of the glass bulk. As for sample 591612, fractures and the central hole are filled with mineralized material, probably coming from the burial soil (Figure 5C). Volume masks corresponding to cracks, soil particles, and glassy material are shown in distinct colors in the 3D rendering of a laboratory μCT scan in Figure 5D. As anticipated, the segmentation of different material phases is easily discernible and more distinct in volume reconstructions derived from SR-μCT phase-contrast data (Figure 5E–G). Consequently, the crack morphology and interconnections can be more thoroughly examined in SR-μCT images. The higher contrast in synchrotron data enables the differentiation of individual particles constituting the sediment within the central hole of the sample (Figure 5H). It is likely that the filling material has mineralized within this confined space.

3.2 | Pitted sample

Sample 591554 displays pit formation as a corrosion phenomenon without any discernible evidence of patina on the surface. This sample was in contact with a soil of higher alkalinity (refer to Table S1 in Supporting Information), where the higher concentration of OH favored the

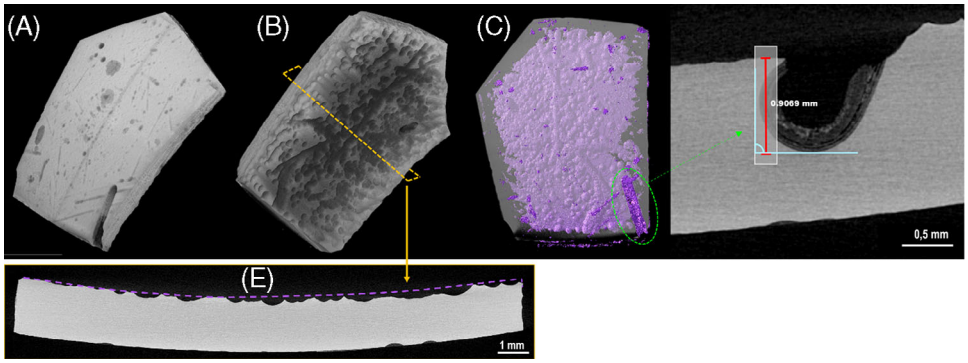

FIGURE 6 3D rendering of the sample 591554: (A) front and (B) back; (C) segmented pits; (D and E) orthogonal tomographic slices of the bigger hole and a middle area with the reference dashed line for pits segmentation, respectively.

dissolution of the Si–O–Si network rather than the leaching of the modifier ions present in the glass matrix.[37] Only laboratory μCT equipment analysis was conducted on this sample.

The surface of the sample displays a nearly complete coverage of interconnected pits of various sizes. The slice in Figure 6E vividly illustrates the distinctly concave profile of these alteration marks. Some pits have dissolved the siliceous matrix to a depth of approximately 0.3 mm, with the largest reaching around 0.9 mm (Figure 6D). By approximating the pits' volume using the ideal purple dashed line in Figure 6E, a tentative segmentation was performed to estimate the quantity of dissolved glassy material. This segmentation employed morphological methods, followed by interpolation in the *x*, *y*, and *z* directions to calculate the entire pits' volume, resulting in an estimation of approximately 11%.

3.3 | Iridescent sample

The initial lower resolution scan of sample 581681 (Figure 7A) aimed to capture the complete and distinctive geometry of this glass fragment. Subsequently, local CT scans were conducted to attain higher resolution images, specifically focusing on the corner, where the multilayered patina exhibits greater thickness. The μCT results provided detailed insights into the thickness, shape, and morphology of the iridescent patina.

The slices presented in Figure 7 reveal the intricate multilayer structure of the overall 1.95-mm thick surface patina (Figure 7B). These images illustrate the organization of various layers within the patina, arranged in packets of differing thicknesses interspersed with zones of air. These air zones appear darker in the images due to their very low absorption coefficient.

Through tomographic reconstructions, it becomes evident how the glass–patina interface and the interfaces among the different layers are discernible. Figure 7C clearly depicts how the profile of the patina mirrors that of the glass, seemingly detaching itself from the bulk of the glass. This structural composition arises from the glass alteration process driven by dissolution and reprecipitation. Initially, water–glass interaction involves the congruent dissolution of the glass until (super)saturation of amorphous silica is attained in a solution boundary layer at the glass surface. The dissolution reactions of the glass are coordinated spatially and temporally with the precipitation of amorphous silica. This synchronization results in the movement of a dissolution–precipitation interface into the glass, leaving behind an altered surface layer composed of amorphous silica. This layer mirrors the initial glass surface.

The CT images also reveal the presence of two pits on the vertical side of the sample (Figure 7D), exhibiting an ordered structure of concentric layers. Recent research[42] discusses various corrosion marks found on tektite glass, including pitting, V-grooves, and U-grooves, which can generally apply to all glass. The pits observed on sample 581681 can be categorized as U-grooves. Their formation is associated with a process unrelated to crack propagation or a corrosion mechanism that operates faster than crack propagation.

Utilizing synchrotron radiation, high-resolution images of the pits along the wall of the glass sample were obtained. The 3D representation of the pit in Figure 7E highlights that some of these structures penetrate through the entire wall of the glass fragment. The well-defined multilayered structure confined within the pit is distinctly visible. This layered arrangement develops due to the cyclical dissolution of the glass network that occurred over centuries.[43]

The tomographic analysis of this iridescent sample unveiled the simultaneous occurrence of two distinct types of glass alteration: additive alteration, resulting in the formation of an iridescent patina, and subtractive alteration, leading to pit formation. Both processes stem

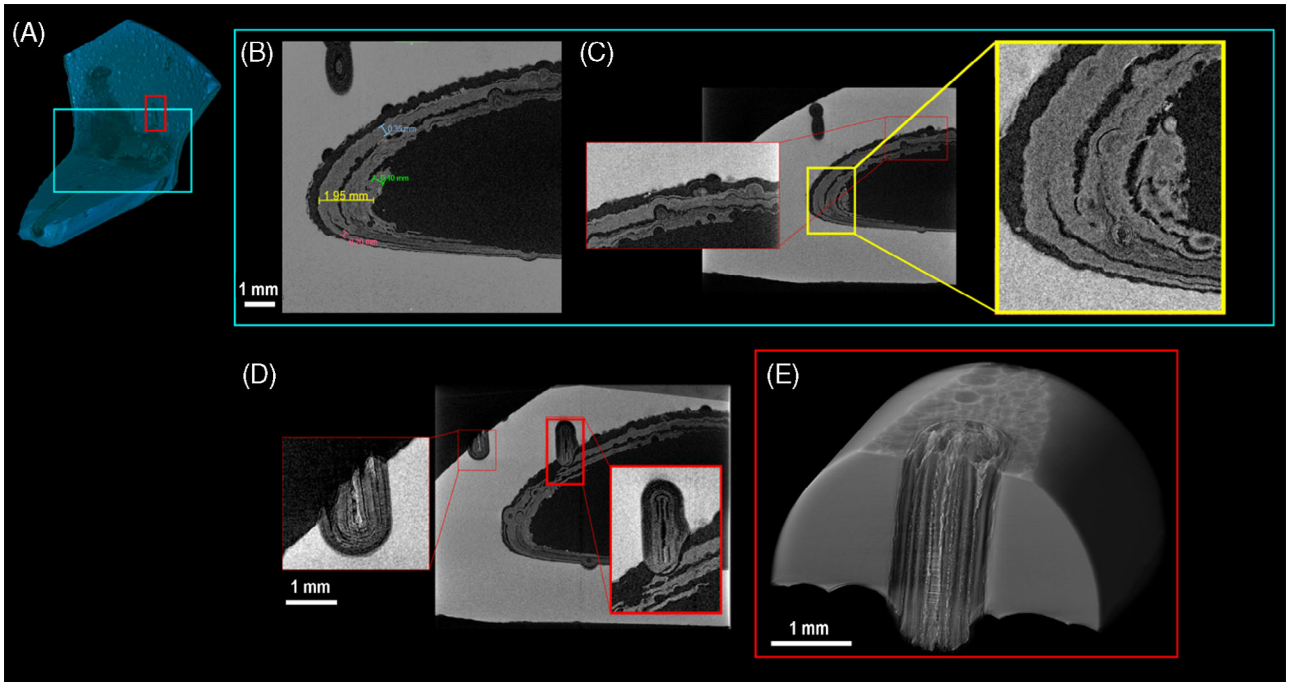

FIGURE 7 (A) 3D rendering of the entire sample; (B and C) tomographic slices of the multilayered patina of the sample 581681 obtained from μCT analysis; (D) tomographic slices of the pit that pass through the vertical wall of the sample 581681 obtained from μCT analysis; (E) 3D rendering of the pit obtained from SR-μCT analysis.

from the interconnected dissolution reactions of the glass, which are coordinated spatially and temporally with the precipitation of amorphous silica.[44]

More precisely, in the context of additive alteration, the development of the iridescent patina represents the culmination of an alteration process instigated in a more acidic environment (pH 6) (refer to Table S1). In this setting, and considering the glass sample composition, we can suppose that the preferential exchange of alkaline ions from the glass matrix with H^+ ions from the surrounding solution—specifically, environmental water present in the soil where the sample has been buried for centuries—has taken place. This ion exchange induces a rise in pH, leading to the breakdown of Si–O bonds within the glass network by OH groups at the solution interface. Consequently, the alteration progresses, culminating in the reorganization of the hydrated glass surface into a densely packed arrangement of silica nanoparticles.[45,46]

Conversely, the formation of pits in the subtractive alteration process arises from the swift dissolution of the Si–O–Si network in an alkaline environment. This is followed by the cyclical organization of hydrated silica layers within the confined space of the pit itself.[47] The presence of salts in the burial soil likely contributes to the localized formation of pits on the surface of the 581681 sample. The accumulation of dissolved salts on the glass surface creates a delimited and isolated area where pH values become highly alkaline.

4 | CONCLUSION

The findings of this study unveil a compelling correlation between the surface and internal morphology of different glass alterations and their documented formation processes. It underscores how the nature of alteration interacts with soil characteristics, confirming distinct changes under defined environmental conditions. Notably, pH emerges as a pivotal factor influencing the evolution of these alterations. These results illuminate the complex interplay among environmental factors, types of alteration, and resultant morphological changes in glass, offering valuable insights for understanding and predicting glass degradation across various scenarios.

In addition, the information collected using CT images of archaeological, cracked glass enabled to understand whether the cracking process is still ongoing, through the propagation of active microcracks that are not visible with 2D imaging techniques. There is no clear evidence of these fractures on archaeological glass in literature, but studying them and understanding how they formed can be of considerable importance in nuclear glass research.

This work, thus, underscores the practical importance of comprehending the long-term alteration processes of ancient glass: this understanding can aid in predicting and managing the durability of specific glass under various environmental conditions and over extended periods. It also provides valuable insights into conservation

strategies for historical glass artefacts and advances the development of more resilient glass materials for modern applications. These insights are crucial for ensuring the enduring stability and longevity of glass in diverse settings.

ACKNOWLEDGMENTS

The authors acknowledge the CERIC-ERIC Consortium for the access to the experimental facility SYRMEP of Elettra (granted proposal no. 20222195) and financial support. The authors take the opportunity to thank the Museo Archeologico Nazionale di Aquileia and Soprintendenza Archeologia, Belle Arti e Paesaggio del Friuli-Venezia Giulia—Superintendency for Archaeology, Fine Arts and Landscape of Friuli—Venezia Giulia Region for research permissions. The μCT analysis have been carried out thanks to the instrumentation available in the OpenAIAr initiative (Associazione Italiana di Archeometria).

Open access publishing facilitated by Istituto Italiano di Tecnologia, as part of the Wiley - CRUI-CARE agreement.

CREDITS

ORCID

Roberta Zanini https://orcid.org/0000-0002-3190-9191
Laura Guidorzi https://orcid.org/0000-0002-6976-1719

REFERENCES

1. Alloteau F, Lehuédé P, Majérus O, Biron I, Dervanian A, Charpentier T, et al. New insight into atmospheric alteration of alkali-lime silicate glasses. Corros Sci. 2017;122:12–25. https://doi.org/10.1016/j.corsci.2017.03.025
2. Alloteau F, Majérus O, Biron I, Lehuédé P, Caurant D, Charpentier T, et al. Temperature-dependent mechanisms of the atmospheric alteration of a mixed-alkali lime silicate glass. Corros Sci. 2019;159:108129. https://doi.org/10.1016/j.corsci.2019.108129
3. Palomar T, Silva M, Vilarigues M, Pombo Cardoso I, Giovannacci D. Impact of solar radiation and environmental temperature on Art Nouveau glass windows. Herit Sci. 2019;7(1):82. https://doi.org/10.1186/s40494-019-0325-3
4. Dal Bianco B, Bertoncello R, Milanese L, Barison S. Surface study of water influence on chemical corrosion of Roman glass. Surf Eng. 2005;21(5–6):393–96. https://doi.org/10.1179/174329305x64376
5. Greiner-Wronowa E, Stoch L. Influence of environment on surface of the ancient glasses. J Non-Cryst Solids. 1996;196:118–27. https://doi.org/10.1016/0022-3093(95)00563-3
6. Palomar T. Effect of soil pH on the degradation of silicate glasses. Int J of Appl Glass Sci. 2017;8(2):177–87. https://doi.org/10.1111/ijag.12226
7. Emami M, Nekouei S, Ahmadi H, Pritzel C, Trettin R. Iridescence in ancient glass: a morphological and chemical investigation. Int J Appl Glass Sci. 2016;7(1):59–68. https://doi.org/10.1111/ijag.12182
8. Vienna JD, Ryan JV, Gin S, Inagaki Y. Current understanding and remaining challenges in modeling long-term degradation of borosilicate nuclear waste glasses. Int J Appl Glass Sci. 2013;4(4):283–94. https://doi.org/10.1111/ijag.12050
9. Alloteau F, Majérus O, Valbi V, Biron I, Lehuédé P, Caurant D, et al. Evidence for different behaviors of atmospheric glass alteration as a function of glass composition. NPJ Mater Degrad. 2020;4(1):36. https://doi.org/10.1038/s41529-020-00138-1
10. Frankel GS, Vienna JD, Lian J, Guo X, Gin S, Kim SH, et al. Recent advances in corrosion science applicable to disposal of high-level nuclear waste. Chem Rev. 2021;121(20):12327–83. https://doi.org/10.1021/acs.chemrev.0c00990
11. Thorpe CL, Neeway JJ, Pearce CI, Hand RJ, Fisher AJ, Walling SA, et al. Forty years of durability assessment of nuclear waste glass by standard methods. NPJ Mater Degrad. 2021;5(1):61. https://doi.org/10.1038/s41529-021-00210-4
12. Gin S, Delaye J-M, Angeli F, Schuller S. Aqueous alteration of silicate glass: state of knowledge and perspectives. NPJ Mater Degrad. 2021;5(1):42. https://doi.org/10.1038/s41529-021-00190-5
13. Zanini R, Franceschin G, Cattaruzza E, Traviglia A. A review of glass corrosion: the unique contribution of studying ancient glass to validate glass alteration models. NPJ Mater Degrad. 2023;7:38. https://doi.org/10.1038/s41529-023-00355-4
14. Janssens K, editor. Modern methods for analysing archaeological and historical glass. 1st ed. Wiley; 2013. https://doi.org/10.1002/9781118314234
15. Verney-Carron A, Gin S, Frugier P, Libourel G. Long-term modeling of alteration-transport coupling: application to a fractured Roman glass. Geochim Cosmochim Acta. 2010;74(8):2291–315. https://doi.org/10.1016/j.gca.2010.01.001
16. Verney-Carron A, Gin S, Libourel G. Archaeological analogs and the future of nuclear waste glass. J Nucl Mater. 2010;406(3):365–70. https://doi.org/10.1016/j.jnucmat.2010.09.028
17. Brancaccio R, Bettuzzi M, Casali F, Morigi MP, Levi G, Gallo A, et al. Real-time reconstruction for 3-D CT applied to large objects of cultural heritage. IEEE Trans Nucl Sci. 2011;58(4):1864–71. https://doi.org/10.1109/TNS.2011.2158850
18. Albertin F, Bettuzzi M, Brancaccio R, Morigi MP, Casali F. x-Ray computed tomography in situ: an opportunity for museums and restoration laboratories. Heritage. 2019;2(3):2028–38. https://doi.org/10.3390/heritage2030122
19. De Chiffre L, Carmignato S, Kruth J-P, Schmitt R, Weckenmann A. Industrial applications of computed tomography. CIRP Ann. 2014;63(2):655–77. https://doi.org/10.1016/j.cirp.2014.05.011
20. Floreani S, Traviglia A, Moretto LM, Bernardoni A. Picking up the hint: raw glass chunks and glass wastes from plough-soil collection in Aquileia (Italy). Poster presented at the 21st International Congress of the Association Internationale pour l'Histoire du Verre, Istanbul, Turkey, September 3–7, 2018.
21. Open AIAr—AIAr. n.d. https://www.associazioneaiar.com/wp/openaiar/
22. Nykonenko D, Yatsuk O, Guidorzi L, Lo Giudice A, Tansella F, Cesareo LP, et al. Glass beads from a Scythian grave on the

island of Khortytsia (Zaporizhzhia, Ukraine): insights into bead making through 3D imaging. Herit Sci. 2023;11(1):238. https://doi.org/10.1186/s40494-023-01078-0
23. Vigorelli L, Croce E, Angelici D, Navone R, Grassini S, Guidorzi L, et al. x-Ray micro-tomography as a method to distinguish and characterize natural and cultivated pearls. Condens Matter. 2021;6(4):51. https://doi.org/10.3390/condmat6040051
24. Tansella F, Vigorelli L, Ricchiardi G, Re A, Bonizzoni L, Grassini S, et al. x-Ray computed tomography analysis of historical woodwind instruments of the late eighteenth century. J Imaging. 2022;8(10):260. https://doi.org/10.3390/jimaging8100260
25. Vigorelli L, Re A, Guidorzi L, Re A, Bonizzoni L, Grassini S, et al. x-Ray imaging investigation on the gilding technique of an ancient Egyptian Taweret wooden statuette. J Imaging. 2021;7(11):229. https://doi.org/10.3390/jimaging7110229
26. Vigorelli L, Re A, Buscaglia P, Manfredda N, Nervo M, Cavaleri T, et al. Comparison of two ancient Egyptian Middle Kingdom statuettes from the Museo Egizio of Torino through computed tomographic measurements. J Archaeol Sci Rep. 2022;44:103518. https://doi.org/10.1016/j.jasrep.2022.103518
27. Vigorelli L, Re A, Guidorzi L, Brancaccio R, Bortolin C, Grassi N, et al. The study of ancient archaeological finds through x-ray tomography: the case of the "Tintinnabulum" from the Museum of Anthropology and Ethnography of Torino. J Phys Conf Ser. 2022;2204(1):012034. https://doi.org/10.1088/1742-6596/2204/1/012034
28. Alarashi H, Benz M, Gresky J, Burkhardt A, Fischer A, Gourichon L, et al. Threads of memory: reviving the ornament of a dead child at the Neolithic village of Ba'ja (Jordan). PLoS One. 2023;18(8):e0288075. https://doi.org/10.1371/journal.pone.0288075
29. Brun F, Massimi L, Fratini M, Dreossi D, Billé F, Accardo A, et al. SYRMEP Tomo Project: a graphical user interface for customizing CT reconstruction workflows. Adv Struct Chem Imaging. 2017;3(1):4. https://doi.org/10.1186/s40679-016-0036-8
30. Kak AC, Slaney M. Principles of computerized tomographic imaging. Society for Industrial and Applied Mathematics; 2001. https://doi.org/10.1137/1.9780898719277
31. Feldkamp LA, Davis LC, Kress JW. Practical cone-beam algorithm. J Opt Soc Am A, JOSAA. 1984;1(6):612–19. https://doi.org/10.1364/JOSAA.1.000612
32. Dragonfly | 3D visualization and analysis solutions for scientific and industrial data | ORS. n.d. Montreal:Comet Technologies Canada.
33. Otsu N. A threshold selection method from gray-level histograms. IEEE Trans Syst Man Cybern. 1979;9(1):62–66. https://doi.org/10.1109/TSMC.1979.4310076
34. Raven C. Numerical removal of ring artifacts in microtomography. Rev Sci Instrum. 1998;69(8):2978–80. https://doi.org/10.1063/1.1149043
35. Paganin D, Mayo SC, Gureyev TE, Miller PR, Wilkins SW. Simultaneous phase and amplitude extraction from a single defocused image of a homogeneous object. J Microsc. 2002;206(1):33–40. https://doi.org/10.1046/j.1365-2818.2002.01010.x
36. Schneider CA, Rasband WS, Eliceiri KW. NIH Image to ImageJ: 25 years of image analysis. Nat Methods. 2012;9(7):671–75. https://doi.org/10.1038/nmeth.2089
37. Gin S, Neill L, Fournier M, Frugier P, Ducasse T, Tribet M, et al. The controversial role of inter-diffusion in glass alteration. Chem Geol. 2016;440:115–23. https://doi.org/10.1016/j.chemgeo.2016.07.014
38. Gin S, Guo X, Delaye J-M, Angeli F, Damodaran K, Testud V, et al. Insights into the mechanisms controlling the residual corrosion rate of borosilicate glasses. NPJ Mater Degrad. 2020;4:41. https://doi.org/10.1038/s41529-020-00145-2
39. Gin S, Jollivet P, Fournier M, Berthon C, Wang Z, Mitroshkov A, et al. The fate of silicon during glass corrosion under alkaline conditions: a mechanistic and kinetic study with the International Simple Glass. Geochim Cosmochim Acta. 2015;151:68–85. https://doi.org/10.1016/j.gca.2014.12.009
40. Geisler T, Nagel T, Kilburn MR, Janssen A, Icenhower JP, Fonseca ROC, et al. The mechanism of borosilicate glass corrosion revisited. Geochim Cosmochim Acta. 2015;158:112–29. https://doi.org/10.1016/j.gca.2015.02.039
41. Koob SP, Van Giffen NAR. Conservation of vitreous materials. In: López Varela SL, editor. The encyclopedia of archaeological sciences. Hoboken, NJ, USA: John Wiley & Sons, Inc.; 2018. p. 1–6. https://doi.org/10.1002/9781119188230.saseas0125
42. Krauss A, Whymark A. The influence of crack propagation on tektite glass corrosion sculpture. Paper presented at: 52nd Lunar and Planetary Science Conference, held virtually, March 15–19, 2021.
43. Schalm O, Nuyts G, Janssens K. Some critical observations about the degradation of glass: the formation of lamellae explained. J Non-Cryst Solids. 2021;569:120984. https://doi.org/10.1016/j.jnoncrysol.2021.120984
44. Gin S, Mir AH, Jan A, Delaye JM, Chauvet E, De Puydt Y, et al. A general mechanism for gel layer formation on borosilicate glass under aqueous corrosion. J Phys Chem C. 2020;124(9):5132–44. https://doi.org/10.1021/acs.jpcc.9b10491
45. Schalm O, Anaf W. Laminated altered layers in historical glass: density variations of silica nanoparticle random packings as explanation for the observed lamellae. J Non-Cryst Solids. 2016;442:1–16. https://doi.org/10.1016/j.jnoncrysol.2016.03.019
46. Guidetti G, Zanini R, Franceschin G, Moglianetti M, Kim T, Cohan N, et al. Photonic crystals built by time in ancient Roman glass. Proc Natl Acad Sci. 2023;120(39):e2311583120. https://doi.org/10.1073/pnas.2311583120
47. Franceschin G, Zanini R, Iori G, Longo E, Divitini G, Tromba G, et al. Non-destructive 3D exploration of silicate glass corrosion: a combined multiscale approach from the macro to the nanoscale. Phys Chem Chem Phys. 2024;26(12):9697–707. https://doi.org/10.1039/D3CP05221D

SUPPORTING INFORMATION

Additional supporting information can be found online in the Supporting Information section at the end of this article.

How to cite this article: Zanini R, Franceschin G, Vigorelli L, Iori G, Chiaberge L, Longo E, et al. Laboratory and synchrotron x-ray micro–computed tomography to shed light on degradation features of corroded Roman glass. J Am Ceram Soc. 2025;108:e20241. https://doi.org/10.1111/jace.20241